Supplemental Information

Electron-Delocalized sp2-N Hybridized Organic Electrode Enables Sustainable and High-Efficiency Electrochemical Ammonium Removal

Haoyuan Qiu,[a] Minjie Shi,[a,]* Peipei Zhang,[a] Yueheng Tao,[a] Xinyue Zhang,[a] Jun Yang,[a] Jingxin Zhao,[b,c]* and Huan Pang[d,]*

[a]School of Materials Science and Engineering, Jiangsu University of Science and Technology, Zhenjiang, Jiangsu, 212003, P. R. China

[b]Nanotechnology Center, School of Fashion and Textiles, The Hong Kong Polytechnic University, Hung Hom, Kowloon, Hong Kong, 999077, P. R. China

[c]Department of Mathematics and Information Technology, The Education University of Hong Kong, Tai Po, New Territories, Hong Kong SAR, 999077, P. R. China

[d]School of Chemistry and Chemical Engineering, Yangzhou University, Yangzhou, Jiangsu, 225009, P. R. China

*Corresponding Author: Prof. M.J. Shi: shiminjie@just.edu.cn;
Prof. J.X. Zhao: jingxzhao@polyu.edu.hk;
Prof. H. Pang: panghuan@yzu.edu.cn

Experimental section

Material synthesis

All raw materials and reagents, including 2,5-dihydroxy-1,4-benzoquinone (DHBQ, ≥98%, Aladdin, CAS 615-94-1) and phenazine-2,3-diyldiamine (TTFQ, ≥95%, Macklin, CAS 655-86-7), were obtained from commercial sources and used without further purification. In a typical synthesis, precisely weighed quantities of 1.40 g (10.0 mmol) DHBQ and 8.41 g (40.0 mmol) TTFQ were combined in an agate mortar and manually ground for 30 min at ambient temperature until achieving a homogeneous mixture. The blended powder was transferred to a quartz reaction vessel, then heated to 160 °C under continuous N_2 flow and maintained for 8 h. After cooling to room temperature, the product was vacuum-filtered, thoroughly washed with deionized water and acetone, then dispersed in 150 mL of 30% HNO_3 (w/w) and refluxed for 2 h with magnetic stirring (500 rpm). The final product was collected by filtration, dried under dynamic vacuum at 60 °C for 12 h, resulting in the formation of the black DHPZ organic compound with a yield of ~71.5%.

Structural characterizations

The morphology and microstructure of samples were evaluated by several characterization techniques, including scanning electron microscope (SEM; FEI Nova NanoSem450), nuclear magnetic resonance spectra (NMR; Bruker Avance III spectrometer, 400 MHz), flourier transform infrared spectrometer (FTIR; Thermo Fisher Scientific Nicolet 6700), ultraviolet-visible spectrophotometer (UV-vis; Shanghai Metash Instruments Co., Ltd UV-8000), X-ray diffraction (XRD; Bruker D8 X-ray spectrometer) equipped with a 2D detector (Cu Kα, λ=1.54 Å), X-ray photoelectron spectroscopy (XPS; KAlpha Thermo electron) and thermal gravimetric analysis (TGA; TGA5500) within an inert atmosphere. All calculations were performed by using the DFT method implemented in the Gaussian 16 program package. The calculations were based on Density Functional Theory (DFT) using the Becke-Lee-Yang-Parr (B3LYP) functional. This combination of method, functional and software was used to derive both the optimized molecular structures and the corresponding vibrational wave numbers for the compounds under investigation. Finite element simulations were conducted using COMSOL Multiphysics software in accordance with the Nernst-Planck equations.[1]

Electrochemical measurements

The constituents of the DHPZ polymer, acetylene black and polyvinylidene fluoride, in a mass ratio of 7:2:1, were combined within an N-methylpyrrolidone (NMP) solvent and agitated continuously to acquire a uniform mixture. Subsequently, this mixture was evenly spread over graphite paper and subjected to drying under vacuum conditions at 60 °C overnight. The electrochemical properties of the DHPZ electrode were performed in 1 M NH_4Cl aqueous electrolyte by using an electrochemical workstation (DH7000C Donghua). In the testing configuration, the as-prepared DHPZ electrode was served as the working electrode, a graphite rod was designated as the counter electrode and a saturated Ag/AgCl electrode was employed for reference purposes. An in-situ Raman study was conducted utilizing a DXR Raman microscope with a 526 nm excitation laser. The 50X objective lens was positioned directly above the optical window, focusing on the DHPZ electrode during the electrochemical process.

GCD tests were measured at different current densities (1~10 A g^{-1}). The specific capacitance (C, F g^{-1}) from the GCD curve can be calculated by the following Eq. S1:

$$C = \frac{I\Delta t}{m\Delta V} \tag{S1}$$

where I (A), Δt (s), ΔV (V) and m (g) correspond to discharging current, discharging time, potential window and active mass of the DHPZ electrode, respectively.

EIS tests were implemented within the frequency range of 100 kHz to 0.01 Hz. The NH_4^+ diffusion process in the DHPZ electrode can be qualitatively calculated by diffusion coefficient (D, cm^2 s^{-1}) according to Eq. S2 and S3:

$$Z' = R_s + R_{ct} + \sigma\omega^{-1/2} \tag{S2}$$

$$D = \frac{R^2T^2}{2A^2n^4F^4C^2\sigma^2} \tag{S3}$$

where Z' and σ are the real part impedance and Warburg factor from the EIS plot, respectively. R, T, A, n, F and C refer to gas constant (8.314 J K^{-1} mol^{-1}), absolute temperature (298 K), electrode surface area (cm^2), number of transferred electrons, faraday constant and NH_4^+ concentration, respectively.

CDI experiments

A CDI device was assembled by using as-prepared DHPZ as anode and commercial activated carbon (AC) as cathode, with an anion exchange membrane placed near the

AC cathode (Zhonglin Tanke Technology Co., LTD) to prevent anion capture during voltage reversal. The CDI device was assembled with several major contents as plexiglass covers (6 × 6 cm^2), rubber gaskets (thickness of 0.3 mm) and current collectors carpeted with active electrode materials (4 × 4 cm^2), the total material weights on anode and cathode were 70 mg. A tank (10 mM, 40 mL) of NH_4Cl aqueous solution was pumped into the assembled CDI device through a peristaltic pump at a fixed flow rate of 10 mL min^{-1}, and then flowed into another tank. The real-time conductivity of the solution was monitored by an online conductivity meter (DDSJ-308F), while the NH_4^+ concentration was calculated by a calibration curve according to the conductivity profiles (Fig. S16).

The NH_4^+ removal behaviors of the assembled CDI device were evaluated by specific removal capacity (*SRC*, mg g^{-1}), average removal rate (*ARR*, mg g^{-1} min^{-1}), charge consumed (Σ, C g^{-1}), charge efficiency (Λ), and energy consumption (E_{con}) according to the following Eq. S4-S8:

$$SRC=\frac{(C_0-C_e)\times V}{m} \tag{S4}$$

$$ARR=\frac{SRC}{t} \tag{S5}$$

$$\Sigma=\frac{\int idt}{m} \tag{S6}$$

$$\Lambda=\frac{SRC\times F}{M_{NH_4^+}\times\Sigma} \tag{S7}$$

$$E_{con}=\frac{U\int idt}{3.6\times SRC\times m} \tag{S8}$$

where C_0 and C_e are the initial and equilibrium final NH_4^+ concentration (mg L^{-1}) calculated according to the conductivity, respectively, V is the volume (L) of NH_4^+ solution, M is the molar mass of NH_4^+, m is the active mass of the DHPZ electrode (g), t is the deammoniation time (s), i is the current during the adsorption process (A), F is Faraday's constant (96485 C mol^{-1}), U is the voltage during the adsorption process (V).

To assess the selectivity coefficient of NH_4^+ relative to other cations, the assembled CDI device was tested at a voltage of 1.2 V in binary salt solutions containing 3.5 mM NH_4Cl mixed with either 3.5 mM NaCl or 3.5 mM $CaCl_2$, and a multi-solution comprising 3.5 mM NH_4Cl together with both 3.5 mM NaCl and $CaCl_2$. The cation concentrations were measured before and after the CDI treatments by using ion chromatography (Essentia IC-16). The selectivity coefficient for the target ion in relation to other species was calculated using the following Eq. S9:

$$S_{i/j} = \frac{\Gamma_i / M_i}{\Gamma_j / M_j} \times \frac{C_{o,i}}{C_{o,j}} \tag{S9}$$

where Γ_i and Γ_j refer to the respective adsorption amounts for i and j ions, respectively; M_i and M_j represent relative atomic masses; and $C_{0,i}$ and $C_{0,j}$ denote the initial concentrations of i and j ions in the feed solution, respectively. In this study, i and j represent the NH_4^+ and other cations (Na^+ and Ca^{2+}), respectively. A $S_{i/j}$ value greater than 1 suggests that NH_4^+ is more preferentially captured than other cations in the CDI device. For practical applications, an integrated electrochemical system was constructed with three interconnected CDI devices that enable multi-stage removal processes. Ammonium wastewater flows into a three-stage CDI treatment system to yield purified water, wherein the realistic wastewater (NH_4^+: 52.69 mg L^{-1}; Na^+: 103.76 mg L^{-1}; K^+: 28.53 mg L^{-1}; Ca^{2+}: 123.45 mg L^{-1}; Mg^{2+}: 45.23 mg L^{-1}; Conductivity: 1482 μS cm^{-1}; pH: ~7.5) collected from municipal wastewater source (Jiangsu region; China). The specific evolutions of NH_4^+ concentrations are determined by ion chromatography.

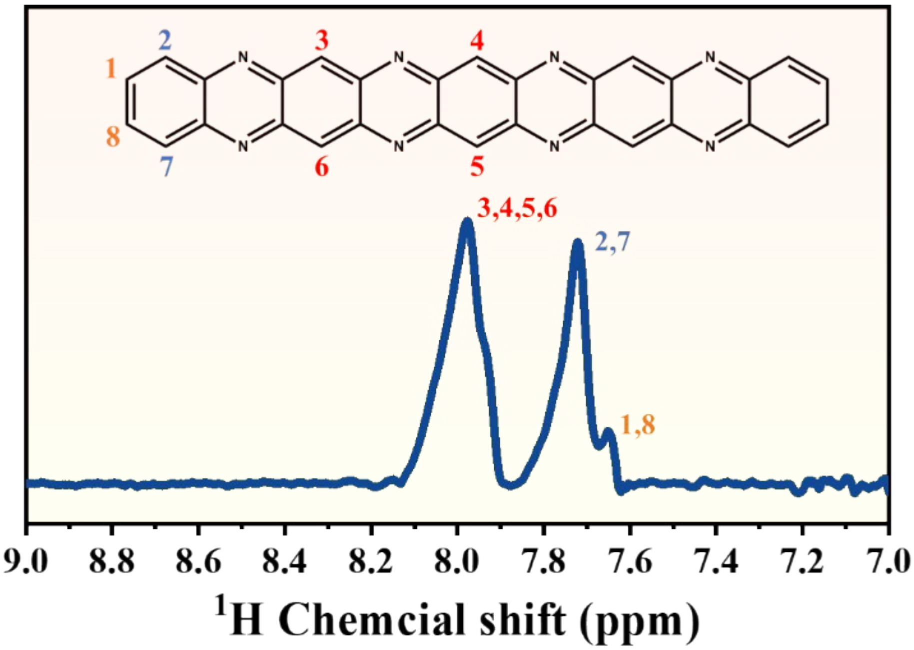

Fig. S1. Liquid-state ^{1}H NMR spectrum of the DHPZ organic matter.

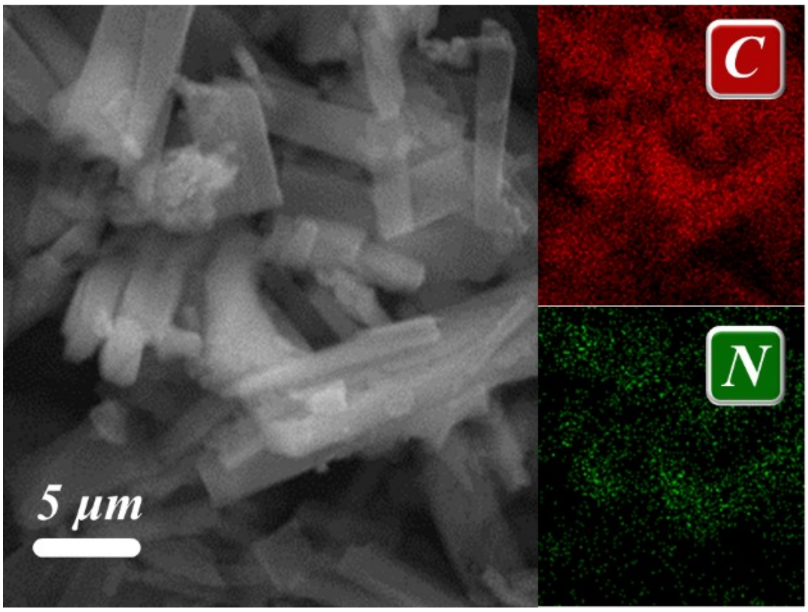

Fig. S2. SEM image and the corresponding EDS mapping images of the DHPZ organic matter with a rod-shaped morphology.

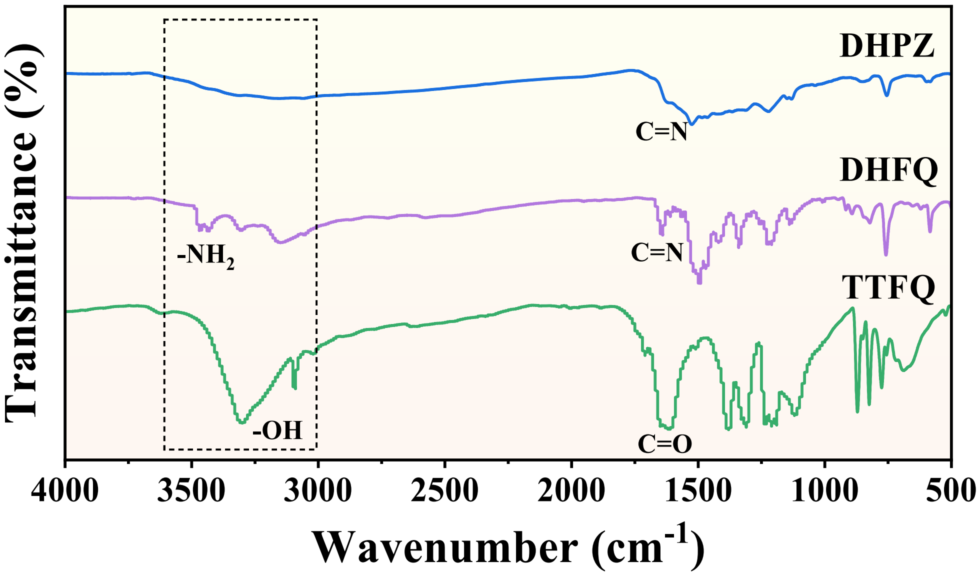

Fig. S3. FT-IR spectra of TTFQ and DHBQ precursors as well as DHPZ product.

As shown in Fig. S3**,** the FT-IR spectra of the DHPZ organic matter reveals an absence of -NH$_2$ and -OH peaks, indicating that the DHPZ can be synthesized through the efficient condensation of the two precursors involving -NH$_2$ and -OH bonds.

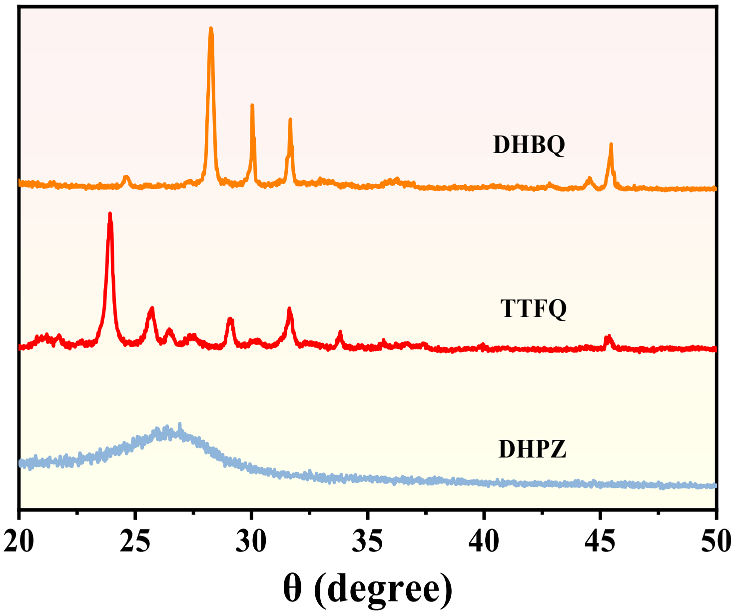

Fig. S4. XRD pattern of TTFQ and DHBQ precursors as well as DHPZ product.

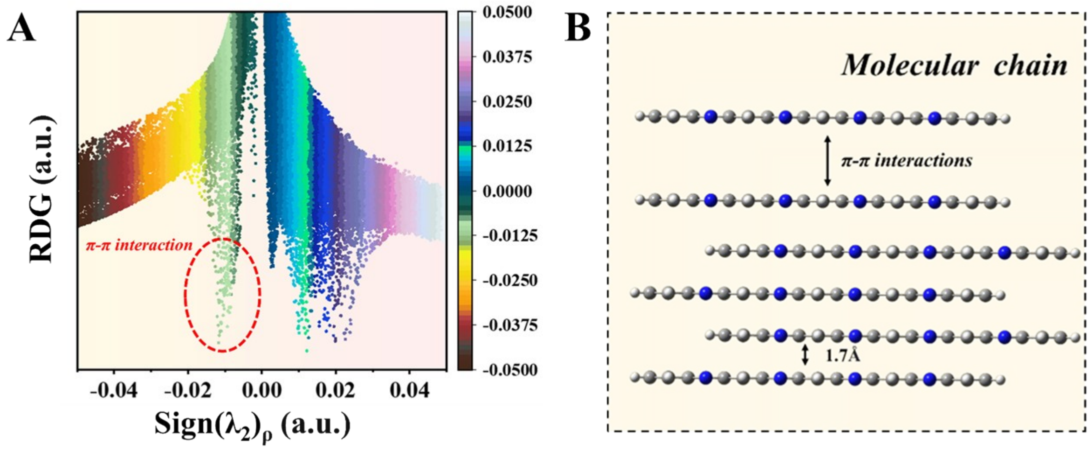

Fig. S5. (A) Plots of RDG vs. sign $(\lambda_2)_\rho$ and (B) the corresponding structural diagram of the DHPZ organic matter via π-π stacking interactions.

X-ray diffraction (XRD) analysis, presented in Fig. S4, reveals distinct structural differences between the DHPZ organic matter and its precursors. While the precursors display sharp and well-defined peaks indicative of a highly crystalline structure, the DHPZ organic matter reveals a broad diffraction peak corresponding to a d-spacing of 1.7 Å, characteristic of π-π stacking interactions between neighboring molecular chains. Further evidence for these interactions is observed in Fig. S5, where a pronounced green spike appears within the sign$(\lambda_2)_\rho$ plot (red dotted circle) in the range of 0 to -0.02 a.u., suggesting substantial π-π interactions between neighboring chains. The prevalence of these robust π-π stacking interactions throughout the DHPZ structure, significantly contributes to the overall molecular stability.

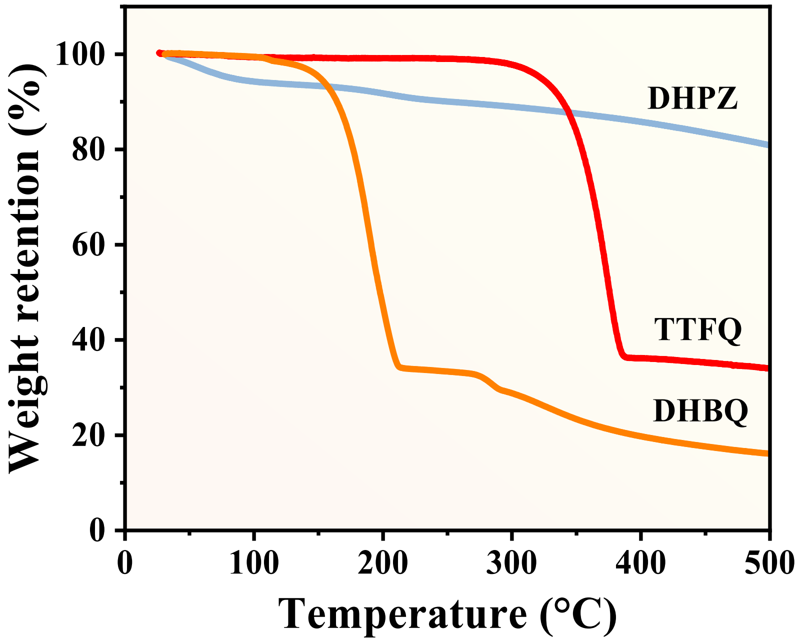

Fig. S6. TGA curves of TTFQ and DHBQ precursors as well as DHPZ product.

As shown in Fig. S6, the as-prepared DHPZ organic matter displays a trifling decrement in mass, preserving a commendable 80.9% of its weight at 500 ℃, illustrating the durability and molecular fortitude of its molecule framework.

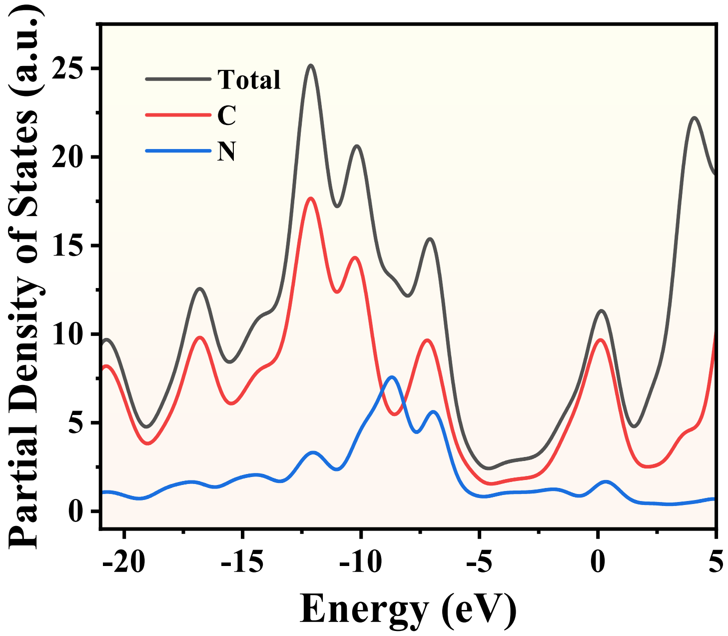

Fig. S7. Partial density of states the DHPZ organic matter.

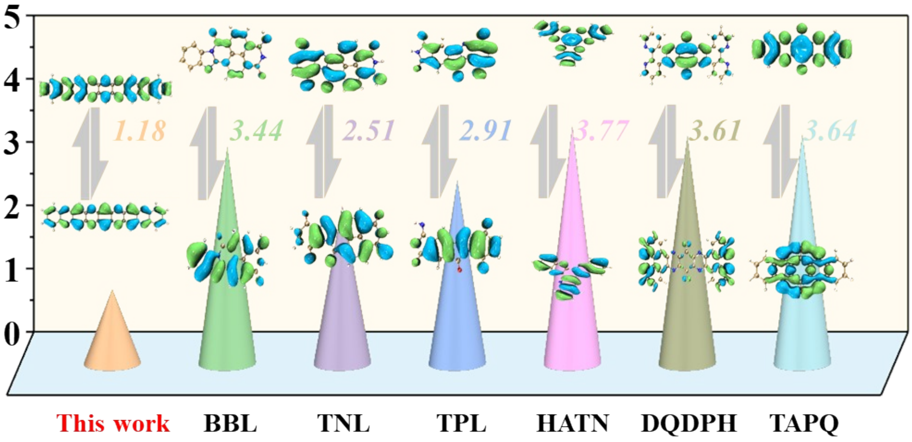

Fig. S8. The comparison of HOMO/LUMO gaps between the DHPZ molecule and typical electroactive organic materials.

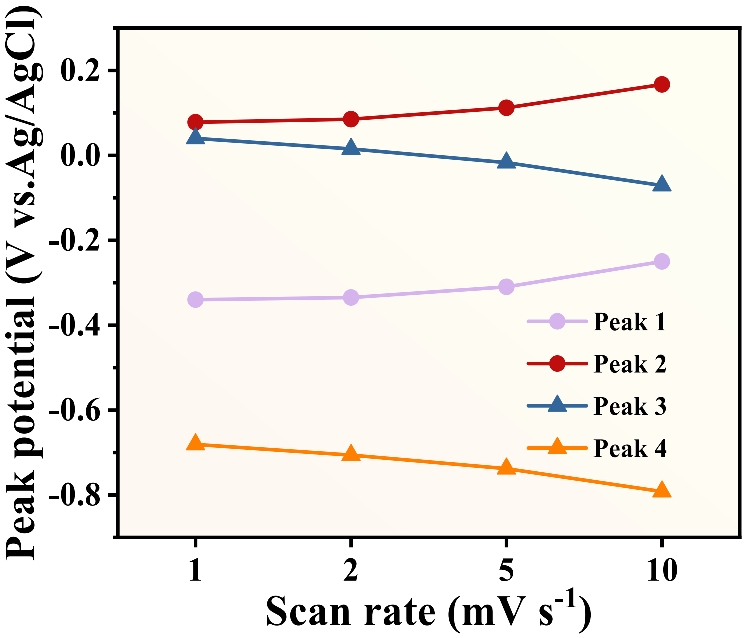

Fig. S9. Peak potentials from CV curves of the DHPZ electrode at various scan rates.

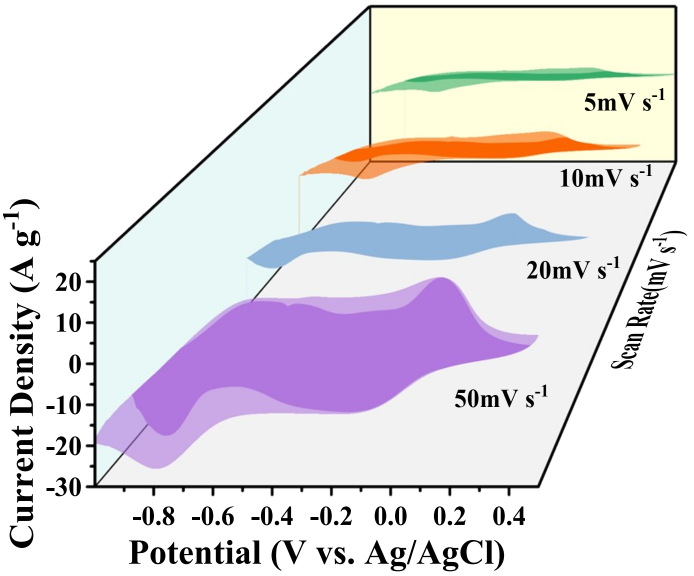

Fig. S10. Voltammetric response with the colored areas representing the capacitive-controlled process of the DHPZ electrode under various scan rates.

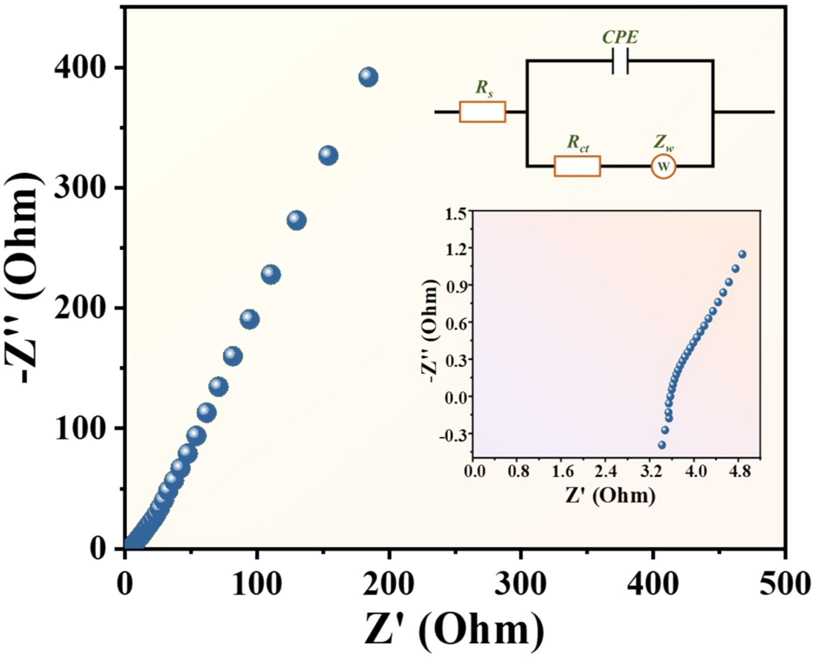

Fig. S11. Nyquist plot of the DHPZ electrode. Inset shows the equivalent circuit diagram.

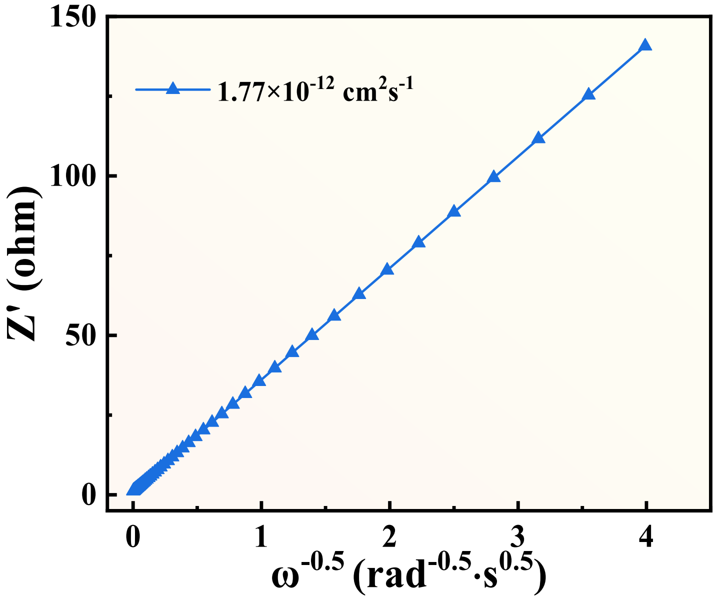

Fig. S12. The corresponding NH_4^+ diffusion coefficient for the DHPZ electrode.

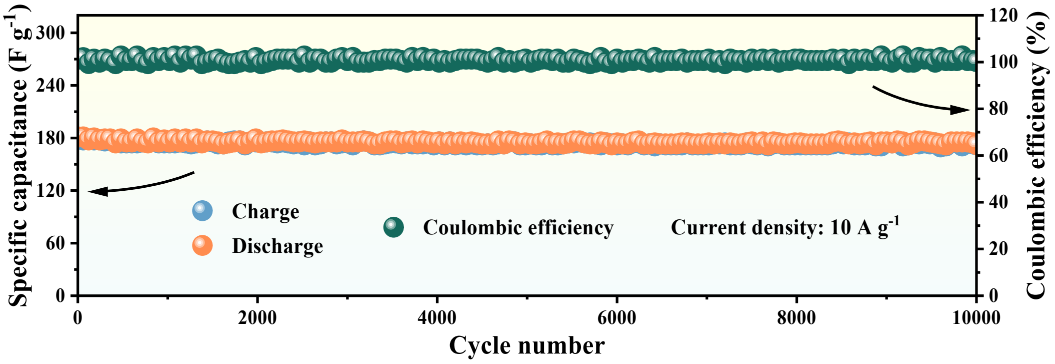

Fig. S13. Long-term cycling stability of the DHPZ electrode at a high current density of 10 A g^{-1}.

To assess the long-term durability of the DHPZ electrode under high-rate operation, prolonged GCD cycling was conducted at 10 A g^{-1} for 10,000 cycles. As shown in Fig. S13, the DHPZ electrode exhibits outstanding electrochemical stability, maintaining 96.27% of its original capacitance after prolonged cycling. This superior cyclability can be attributed to the inherent structural robustness of the DHPZ electrode, which effectively resists degradation even under demanding high-current conditions.

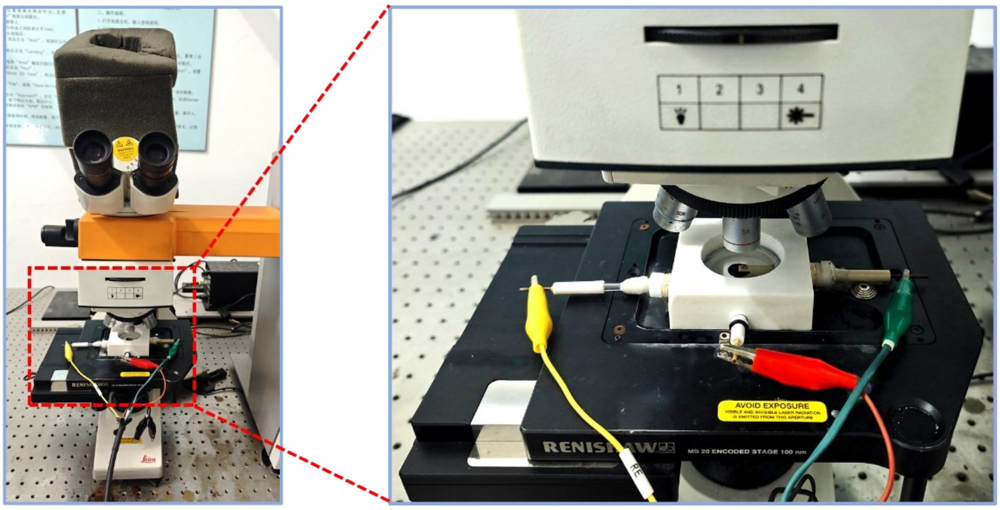

Fig. S14. Digital photo of the in-situ Raman apparatus integrated with electrochemical measurement.

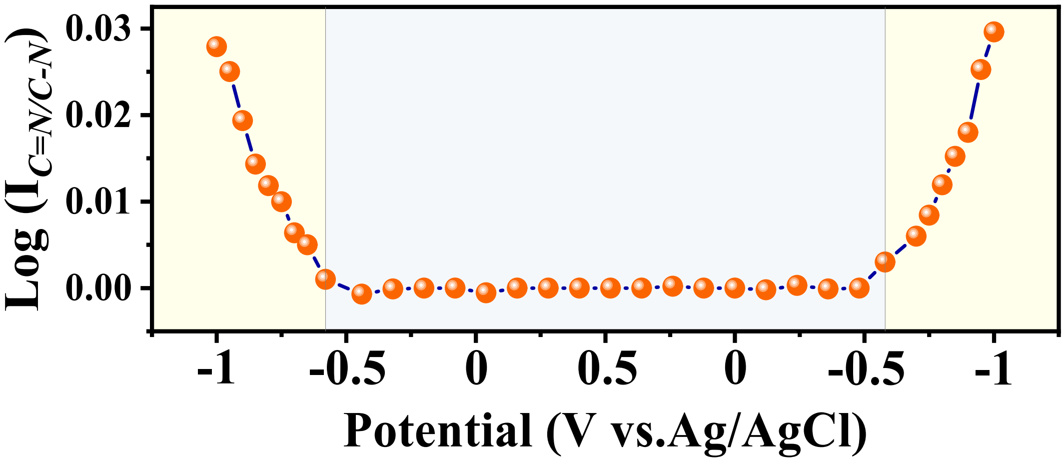

Fig. S15. The ratio of peak intensities for the C=N and C-N bonds ($I_{C=N}/I_{C–N}$) from in-situ Raman spectra upon NH_4^+ uptake and release.

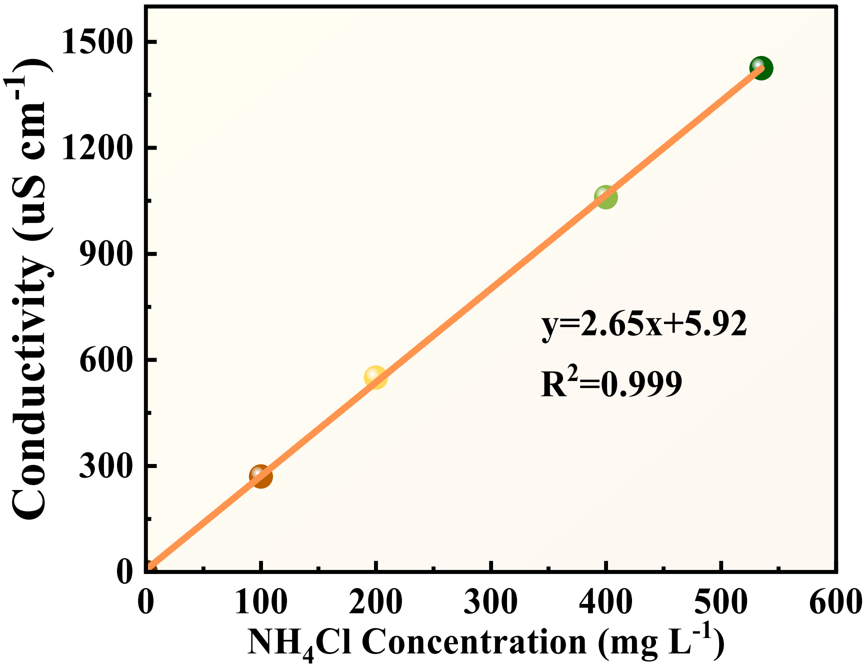

Fig. S16. The relationship between NH_4Cl concentration and conductivity.

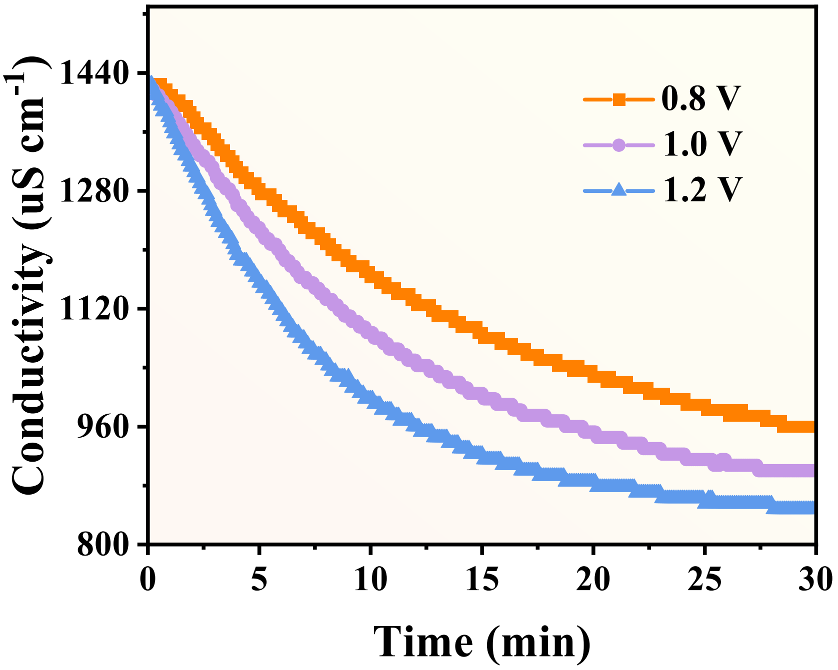

Fig. S17. The variations in solution conductivity during the CDI treatments under different applied voltages.

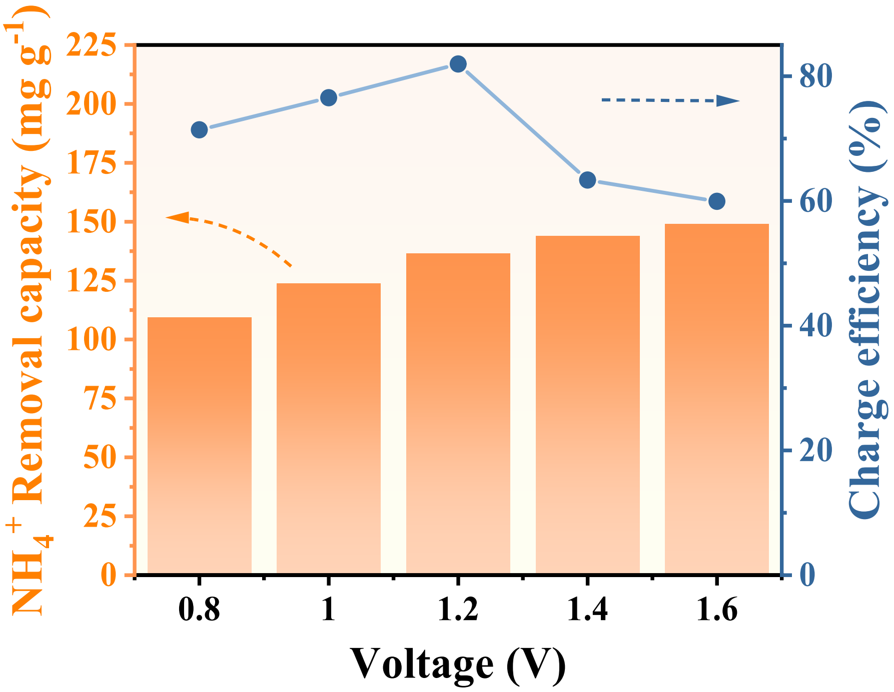

Fig. S18. The NH_4^+ removal capacities and the corresponding charge efficiencies of the CDI device under different applied voltages.

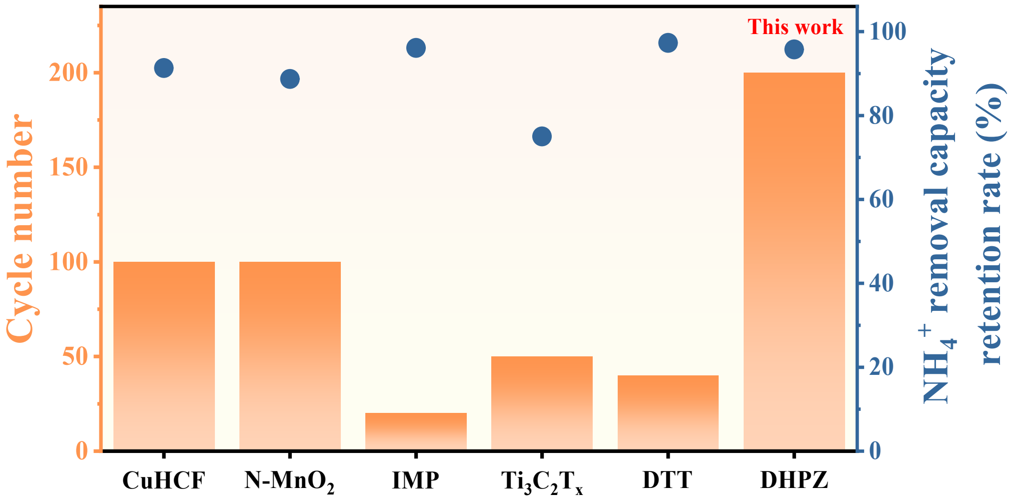

Fig. S19. Comparison of the regeneration performance of our proposed CDI device against other reported CDI devices for NH_4^+ removal.[2-6]

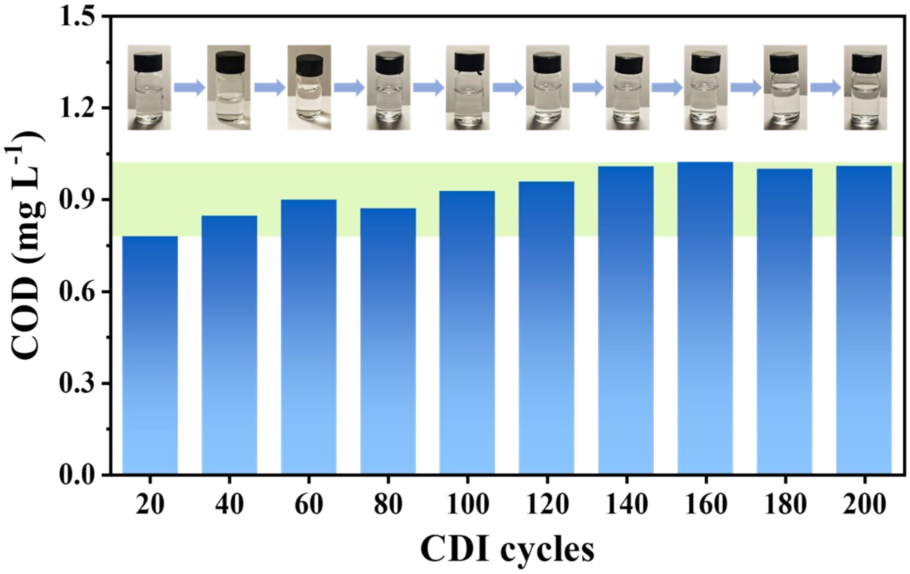

Fig. S20. The COD values of NH_4Cl solution monitored during repeated CDI processes at an applied voltage of 1.2 V.

To systematically assess potential leaching of organic components from the DHPZ electrode during operation, we have performed chemical oxygen demand (COD) measurements at regular intervals throughout multiple CDI cycles. Using a colorimetric detection method with UV-vis spectrophotometry, we can observe consistently low COD values ranging from 0.78 to 1.01 mg L^{-1} (Fig. S20). These minimal and stable COD levels indicate negligible dissolution of organic matter from the DHPZ electrode into the aqueous phase. The results confirm the exceptional structural integrity and chemical stability of the DHPZ organic framework during extended CDI operation, highlighting its high potential for sustainable and long-term CDI applications.

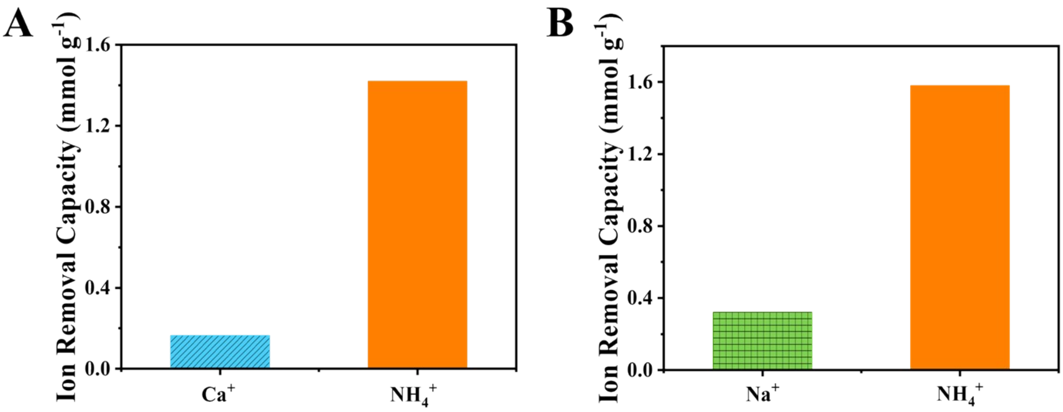

Fig. S21. Ion removal capacities of CDI device in binary salt solutions: (A) 3.5 mM NH_4^+ and 3.5 mM Ca^{2+}, (B) 3.5 mM NH_4^+ and 3.5 mM Na^+.

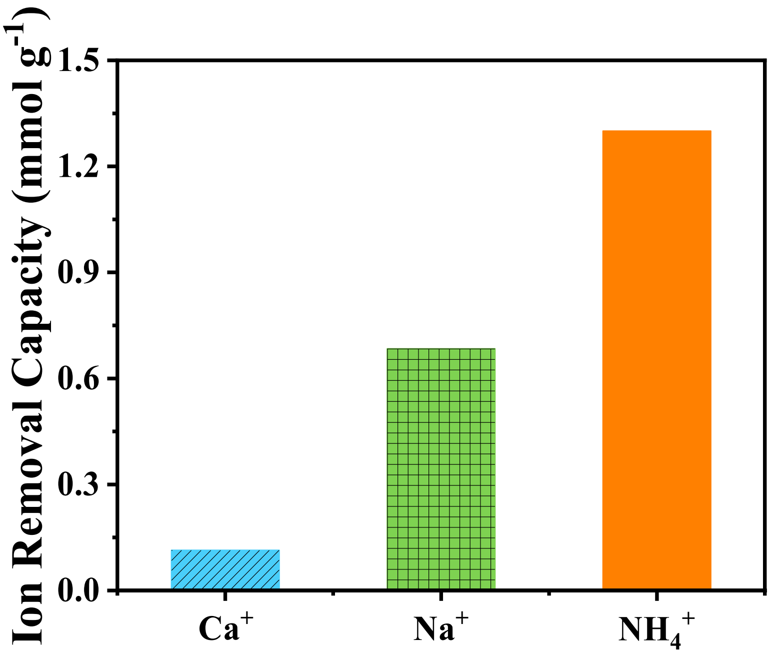

Fig. S22. Ion removal capacities of CDI device in a multi-solution: 3.5 mM NH_4^+ together with both 3.5 mM Na^+ and 3.5 mM Ca^{2+}.

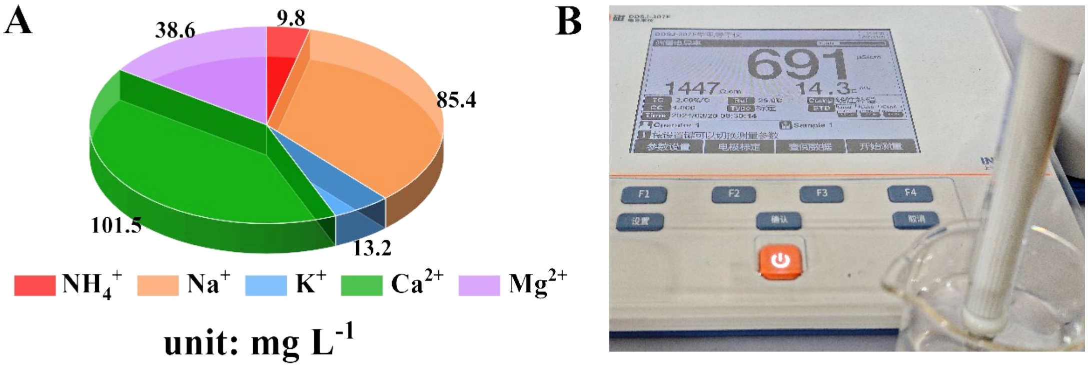

Fig. S23. (A) Concentrations of cations and (B) conductivity of the treated effluent following system processing.

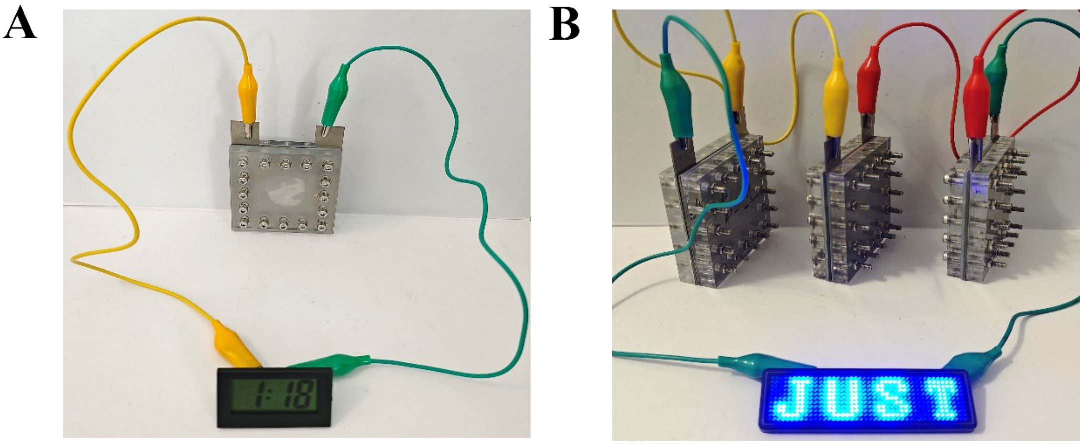

Fig. S24. Energy recovery of (A) a CDI device and (B) three CDI devices interconnected in series during the discharge process.

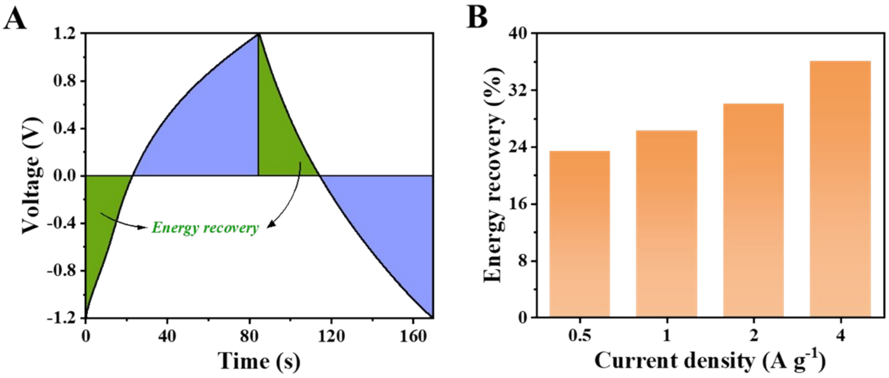

Fig. S25. (A) Voltage changes of the CDI device during charging and discharging. (B) Energy recovery efficiencies at different current densities.

The energy recovery performance of the CDI device was systematically evaluated through GCD measurements across an operational potential window of -1.2 to 1.2 V. As illustrated in Fig. S25A, two distinct operational modes were identified: (1) energy recovery phases, corresponding to voltage transitions from -1.2 V to 0 V and 1.2 V to 0 V (denoted by green regions), and (2) energy consumption phases, occurring during voltage shifts from 0 V to 1.2 V and 0 V to -1.2 V (indicated by blue regions). Notably, our analysis reveals a strong positive correlation between current density and energy recovery efficiency, with higher current densities yielding significantly enhanced performance (Fig. S25B). Particularly impressive is the device's achievement of a 36.13% energy recovery rate at 4 A g^{-1}, demonstrating its considerable promise for practical applications in sustainable energy recovery systems.

Table S1. Cycle performances of our proposed DHPZ electrode with the existing NH_4^+-capture electrodes.

Electrode material	**Retention rate**	**Cycle number**	**Electrolyte**	**Ref.**
BG	78%	50000	0.5 M $(NH_4)_2SO_4$	7
PVO	42%	100	0.5 M $(NH_4)_2SO_4$	8
SR-CoFe LDHs	90.4%	10000	0.5 M $(NH_4)_2SO_4$	9
PNFF	95.2%	1000	1 M $(NH_4)_2SO_4$	10
FeMnHCF	68.5%	10000	1 M $NH_4CF_3SO_3$	11
$NH_4V_4O_{10}$	92.8%	3000	5 M $(NH_4)_2SO_4$	12
Ni-APW	74%	2000	1 M $(NH_4)_2SO_4$	13
Mn_3Al_1-LDH	81%	400	0.5 M $(NH_4)_2SO_4$	14
DHPZ	**95.93%**	**10000**	**1 M NH_4Cl**	**This work**

Table S2. Comparison of NH_4^+ removal performances with advanced CDI devices based on various electrode materials.

	Electrode materials	**Imposed voltage**	**NH_4^+ removal capacity**	**Regeneration stability**	**Ref.**
Carbon derivatives	Graphite	1.2 V	1.43	1.43 mg g^{-1} after 4 cycles	15
	Graphene Laminates	2.0 V	15.31	15.31 mg g^{-1} after 4 cycles	15
Metal-based materials	N-MnO_2-x	1.4 V	134.31	119.13 mg g^{-1} after 100 cycles	3
	$Ti_3C_2T_x$	1.4 V	39.7	29.775 mg g^{-1} after 50 cycles	5
	CeO_2	1.2 V	7.66	NA	16
	TiO_2	2.0 V	8.52	8.02 mg g^{-1} after 10 cycles	17
Prussian blue analogues	NiHCF	1.2 V	36.2	NA	18
	CuHCF	1.2 V	120.2	109.77 mg g^{-1} after 100 cycles	2
	ZnHCF	1.2 V	40.7	48.1 mg g^{-1} after 100 cycles	19
Organic compounds	IMP	1.2 V	119	114.359 mg g^{-1} after 20 cycles	4
	DTT	1.2 V	72.1	70.15 mg g^{-1} after 40 cycles	6
	DHPZ	**1.2 V**	**136.6 mg g^{-1}**	**130.8 mg g^{-1} after 200 cycles**	**This work**

References

1. J. Wu, X. Xuan, S. Zhang, Z. Li, H. Li, B. Zhao, H. Ye, Z. Xiao, X. Zhao, X. Xu, X. Liu, J. You and Y. Yamauchi, *Chem. Eng. J.*, 2023, **473**, 145421.
2. S. Wang, Z. Pan, Z. Li, H. Zhuang, L. Zhao, Z. Li, Y. Lei and G. Wang, *Chem. Eng. J.*, 2023, **466**, 143163.
3. S. Wang, L. Zhao, Y. Lei, Z. Li and G. Wang, *Sep. Purif. Technol.*, 2024, **329**, 125204.
4. J. Jin, R. Wang, K. Yu, Y. Tao, P. Zhang, L. Ke, J. Yang and M. Shi, *Sep. Purif. Technol.*, 2025, **353**, 128290.
5. T. K. A. Nguyen, N. T. N. Anh, M. D. Nguyen, V. T. Nguyen and R. Doong, *Sep. Purif. Technol.*, 2023, **327**, 124934.
6. X. Zhao, J. Yang, J. Peng, Y. Liu, H. Zhang, C. Yan and M. Shi, *Desalination*, 2024, **592**, 118120.
7. X. Wu, Y. Xu, H. Jiang, Z. Wei, J. J. Hong, A. S. Hernandez, F. Du and X. Ji, *ACS Appl. Energ. Mater.*, 2018, **1**, 3077-3083.
8. C. Han, J. Zhu, K. Fu, D. Deng, W. Luo and L. Mai, *Chem. Commun.*, 2022, **58**, 791-794.
9. D. Wang, J. Sun and L. Chen, *ChemSusChem*, 2023, **16**, e202300207.
10. W. Hou, C. Yan, P. Shao, K. Dai and J. Yang, *Nanoscale*, 2022, **14**, 8501-8509.
11. L. Du, S. Bi, M. Yang, Z. Tie, M. Zhang and Z. Niu, *PNAS*, 2022, **119**, e2080422177.
12. S. Li, D. Yu, J. Liu, N. Chen, Z. Shen, G. Chen, S. Yao and F. Du, *Adv. Sci.*, 2023, **10**, 2206836.
13. X. Wu, Y. Qi, J. J. Hong, Z. Li, A. S. Hernandez and X. Ji, *Angew. Chem. Int. Ed.*, 2017, **56**, 13026-13030.
14. Q. Liu, F. Ye, K. Guan, Y. Yang, H. Dong, Y. Wu, Z. Tang and L. Hu, *Adv. Energy Mater.*, 2023, **13**, 2202908.
15. Y. Wimalasiri, M. Mossad and L. Zou, *Desalination*, 2015, **357**, 178-188.

16. B. Xu, K. Jiang, Y. Gan, K. Zhang, J. Zhang, J. Luo, H. Xu, Z. Chen, W. Yang, H. Li and X. Lu, *J. Water Process. Eng.*, 2024, **58**, 104912.
17. B. Xu, X. Xu, H. Gao, F. He, Y. Zhu, L. Qian, W. Han, Y. Zhang and W. Wei, *Sep. Purif. Technol.*, 2020, **250**, 117243.
18. S. Tsai, D. V. Cuong and C. Hou, *Water Res.*, 2022, **221**, 118786.
19. Q. Wang, Q. Wu, M. Zhao, S. Lu and D. Liang, *Chem. Eng. J.*, 2024, **482**, 148923.